Research paper

Modeling excitability in cerebellar stellate cells: Temporal changes in threshold, latency and frequency of firing

John Mitry [a], Ryan P.D. Alexander [b], Saeed Farjami [a], Derek Bowie [b], Anmar Khadra [a],[*]

[a] Department of Physiology McGill University McIntyre Medical Building 3655 Promenade Sir William Osler, Montréal, QC H3G 1Y6, Canada
[b] Department of Pharmacology and Therapeutics McGill University, Montréal, QC, Canada

ABSTRACT

Cerebellar stellate cells are inhibitory molecular interneurons that regulate the firing properties of Purkinje cells, the sole output of cerebellar cortex. Recent evidence suggests that these cells exhibit temporal increase in excitability during whole-cell patch-clamp configuration in a phenomenon termed runup. They also exhibit a non-monotonic first-spike latency profile as a function of the holding potential in response to a fixed step-current. In this study, we use modeling approaches to unravel the dynamics of runup and categorize the firing behavior of cerebellar stellate cells as either type I or type II oscillators. We then extend this analysis to investigate how the non-monotonic latency profile manifests itself during runup. We employ a previously developed, but revised, Hodgkin–Huxley type model to show that stellate cells are indeed type I oscillators possessing a saddle node on an invariant cycle (SNIC) bifurcation. The SNIC in the model acts as a "threshold" for tonic firing and produces a slow region in the phase space called the ghost of the SNIC. The model reveals that (i) the SNIC gets left-shifted during runup with respect to $I_{app} = I_{test}$ in the current-step protocol, and (ii) both the distance from the stable limit cycle along with the slow region produce the non-monotonic latency profile as a function of holding potential. Using the model, we elucidate how latency can be made arbitrarily large for a specific range of holding potentials close to the SNIC during pre-runup (post-runup). We also demonstrate that the model can produce transient single spikes in response to step-currents entirely below I_{SNIC}, and that a pair of dynamic inhibitory and excitatory postsynaptic inputs can robustly evoke action potentials, provided that the magnitude of the inhibition is either low or high but not intermediate. Our results show that the topology of the SNIC is the key to explaining such behaviors.

© 2019 Elsevier B.V. All rights reserved.

1. Introduction

Cerebellar stellate cells are GABAergic interneurons located in the superficial molecular layer of the cerebellar cortex [25] which have roles in shaping motor behavior in vivo [12]. Their primary inputs are glutamatergic parallel fiber synapses and GABAergic activity from adjacent molecular layer interneurons [16], but they also receive excitatory input

through glutamate spillover from climbing fiber-Purkinje cell synapses [33]. They are spontaneously active at rest [13,19] and their output inhibits the firing of Purkinje cells [13], the principal output of the cerebellar cortex. Because of their high input resistance, stellate cells are strongly influenced by minimal amounts of synaptic input [8], and it has been suggested that there are also potential technical confounds when their activity is measured [1].

In the absence of any synaptic input, stellate cells are spontaneously active, tonically firing action potentials (AP) with frequencies ranging from $5 - 30$ Hz [5,23]. In fact, recent experimental evidence [1,3] has shown that these neurons experience a temporal change in their intrinsic excitability in a phenomenon called runup. This phenomenon is characterized by an increase in spontaneous and step-evoked firing frequency and a decrease of AP threshold, during the first 25 minutes of whole-cell patch-clamp recording [3]. They also exhibit a non-monotonic profile in their first spike latency when plotted as a function of the holding potential of the cell [23], defined as the membrane potential below the firing threshold induced when a hyperpolarizing current is applied. Differences in $v_{1/2}$ of the steady-state inactivation of the A-type K$^+$ and low threshold T-type Ca^{2+} channels are implicated in producing this non-monotonic profile. In the rodent cerebellum, these two channels appear to form a signaling complex that efficiently couples calcium influx to K$^+$ channel-interacting proteins (which contain calcium-binding domains) to modulate A-type channels [5] and to enable an adaptive regulation of inhibitory input to Purkinje cells during fluctuations in extracellular Ca^{2+} [4]. They also play key roles in generating arbitrarily low tonic spiking frequency in the frequency-applied current ($f - I$) plot for stellate cells consistent with that seen in type I oscillators [7,14,23]. Importantly, the electrophysiological data used to demonstrate these results were most likely collected $25 - 30$ min after patch-clamping the cell. One can thus assume that the electrical activities recorded by these neurons are in the post-runup phase of recordings (i.e., after the increase in excitability) rather than in the pre-runup phase (i.e., before the increase in excitability). Determining how the non-monotonic first-spike latency profile manifests itself in the context of runup (pre versus post) and how oscillations by these neurons are characterized during runup remain open questions.

A Hodgkin–Huxley type model was previously developed to study the dynamics of excitability in stellate cells, particularly the role of A-type K$^+$ and T-type Ca^{2+} [5,20,26,30] channels in producing the non-monotonic profile in first-spike latency [23]. The model showed how these two currents interact to produce only $\sim 60\%$ increase in first-spike latency at the peak of the non-monotonic profile, which is lower than $\sim 100\%$ increase seen experimentally. The results nonetheless validate the role of inactivation kinetics of the A-type K$^+$ and T-type Ca^{2+} in generating such outcomes. The role of A-type K$^+$ channel in producing monotonic increase in latency has been previously documented experimentally [17,32] and investigated mathematically [15]. Interestingly, it was shown that in a Hodgkin–Huxley model that additionally includes an A-type K$^+$ channel, one can observe a monotonic increase in latency as a function of the holding potential and that the timing of a brief excitatory pulse during the generation of the first AP, after the application of a depolarizing applied current, produces a minimum time below of which latency cannot be reduced [29]. Unlike the model in [23], it was shown using slow-fast analysis that the model is a type II oscillator [7,11,14] possessing a subcritical Hopf that produces the "ramp" phenomenon (in which solution trajectories stay close to the unstable steady state for extended period of time after crossing the Hopf bifurcation before they get repelled to the limit cycle) upon increasing the time constant of inactivation for the A-type K$^+$ channel [29]. These studies highlight the key role of A-type K$^+$ channel in affecting latency to first spike.

One fundamental difference between type I and type II excitability is that the former produces arbitrarily low frequency firing in the $f - I$ curve while the latter has a minimum firing frequency well above 0 Hz [11]. The presence of a saddle node on an invariant cycle (SNIC) bifurcation, where a homoclinic bifurcation meets a saddle-node bifurcation, in type I oscillators is responsible for generating these arbitrarily low firing frequencies [27] and spike-frequency adaptation [10,31]. Such topology differs from the Hopf bifurcation seen in type II oscillators [11]. Using a two-dimensional phenomenological model that possesses a SNIC bifurcation [15], one can show that a slow region close to the SNIC (also called ghost of the SNIC) can be formed causing solution trajectories that pass through it to slow down with a passage time proportional to $1/(\sqrt{|I_{app} - I_{SNIC}|})$, where I_{SNIC} and I_{app} are the magnitudes of the depolarizing step-currents landing at the SNIC and beyond, respectively. This type of critical slowing down of solution trajectories is reminiscent to those seen in other neuronal models that possess saddle-node bifurcations coalescing with a homoclinic orbit [21,24]. One particular example of such models is the two-compartment (dendrites and soma) ghostburster model describing the dynamics of electrosensory lateral line lobe (ELL) of weakly electric fish [9,18].

Although the Hodgkin–Huxley type model in [5,23] is designed to capture post-runup recordings, comparing the AP-cycle plotted in the $(V, dV/dt)$-plane, several major discrepancies appear between the cycles produced by the model and data. In fact, very few features of the cycles of AP produced by the model are in common with the pre- and post-runup AP-cycle data. Using a careful fitting approach [3], the model parameters have been adjusted to capture both sets of data (pre- and post-runup). Here, we analyze the dynamic properties of this revised model with the new set of parameters and identify the role of the SNIC in producing the pre- and post-runup behaviors. We extend this study to examine the non-monotonic first-spike latency during both pre- and post-runup and show that, in certain cases, one can obtain single transient spikes near the SNIC as well as latencies that can become arbitrarily large closer to the SNIC. The single-spike phenomenon is dynamically different from the single transient bursting behavior seen near a SNIC in a generic model of the leech heart interneuron generated in response to a brief inhibitory current pulse [6]. We finally show how the model responds to synaptic (dynamic) inputs during pre- and post-runup.

2. Methods

2.1. Cerebellar stellate cell runup model

A model of cerebellar stellate cells electrical activity presented in [5,23] is adapted to study the runup phenomenon. This model was constructed as a non-specific spiking mechanism (including Na^+, K^+ and leak currents) to which two cerebellar stellate cell specific currents are added, including the A-type K^+ and the T-type Ca^{2+} currents [20,26,30]. The resulting model is a six-dimensional Hodgkin–Huxley type model given by the following system of equations.

$$
\begin{aligned}
C_{\mathrm{m}} \frac{dV}{dt} &= -I_{\mathrm{Na}} - I_{\mathrm{K}} - I_{\mathrm{L}} - I_{\mathrm{A}} - I_{\mathrm{T}} + I_{\mathrm{app}} \\
\frac{dx}{dt} &= \frac{(x_{\infty}(V) - x)}{\tau_x(V)}, \qquad\qquad x = h,\, n,\, n_{\mathrm{A}},\, h_{\mathrm{A}},\, h_{\mathrm{T}},
\end{aligned}
\tag{1}
$$

where C_{m} is the membrane capacitance (in $\mu F/cm^2$), I_η, η=Na, K, L, A, T, are the ionic currents defined by

$$
\begin{aligned}
I_{\mathrm{Na}} &= g_{\mathrm{Na}}\, m_{\infty}^3\, h\, (V - E_{\mathrm{Na}}) \\
I_{\mathrm{K}} &= g_{\mathrm{K}}\, n^4\, (V - E_{\mathrm{K}}) \\
I_{\mathrm{L}} &= g_{\mathrm{L}}\, (V - E_{\mathrm{L}}) \\
I_{\mathrm{A}} &= g_{\mathrm{A}}\, n_{\mathrm{A}}\, h_{\mathrm{A}}\, (V - E_{\mathrm{K}}) \\
I_{\mathrm{T}} &= g_{\mathrm{T}}\, m_{\mathrm{T},\infty}\, h_{\mathrm{T}}\, (V - E_{\mathrm{Ca}}),
\end{aligned}
\tag{2}
$$

$x = h, n, n_{\mathrm{A}}, h_{\mathrm{A}}, h_{\mathrm{T}}$ are the gating variables (unitless) and τ_x are the time constants (in ms). The two parameters, g_η and E_η, appearing in Eq. (2) denote, respectively, maximum ionic conductances (in $\mu S/cm^2$) and reversal potentials (in mV). As suggested by these equations, the gating variables for activation m and m_{T} are fast and therefore set to their steady states. The steady-state activation/inactivation function for each ionic current is given by a sigmoid function of the form

$$
x_{\infty}(V) = \frac{1}{1 + e^{-(V - v_x)/s_x}},
$$

where v_x and s_x are in mV. Furthermore, the time constant for sodium current inactivation is described by a Lorentzian function, defined by

$$
\tau_h(V) = y_0 + \frac{2Aw}{4\pi (V - V_c)^2 + w^2},
$$

whereas the time constant for delayed rectifier potassium current activation is described by a sigmoid function, given by

$$
\tau_n(V) = \frac{6}{1 + e^{(V+23)/15}}.
$$

2.2. Model fitting and parameter estimation

The electrophysiological data presented in [23] were collected tens of minutes after patch clamping cerebellar stellate cells (i.e., post-runup). Although the values of model parameters used in [5,23] were able to reproduce salient features of the latency to first spike in these cells in response to a sub- to suprathreshold current-step protocol, the cycles of AP generated by the same model did not match very well the experimental cycles obtained during pre- (at $t = 0$ min) and post-runup (at $t = 25$ min) (see Fig. 1). We have therefore adapted the same model, given by Eqs. (1)–(2), by leaving the currents unchanged and fitting the model to experimental data obtained for pre-runup ($t = 0$ min) and post-runup ($t = 25$ min).

Our method of data fitting makes use of two diagnostics: (1) tonic spiking frequency, and (2) the "shape" of the AP plotted as a cycle in the $(V, dV/dt)$-plane. Fig. 2 provides a comparison of data to the model showing both diagnostics. To fit the model to two independent sets of data, we first fit the model to the data set obtained at $t = 0$ min. We then fit the model to the second data set by varying only steady-state activation and inactivation kinetics. The latter is informed by the underlying physiology, based on the hypothesis that changes in activation/inactivation steady-states cause runup [3].

Parameter values associated with each ionic current for pre- and post-runup obtained using this method of estimation are provided in Table 1. The remaining parameters are provided in Table 2.

2.3. Software

Model simulations have been performed using MATLAB 2017b and XPP (a freeware by Bard Ermentrout available online: http://www.math.pitt.edu/~bard/xpp/xpp.html) and bifurcation analyses have been computed by Auto (a freeware, originally developed by Eusebius Doedel, available online: http://cmvl.cs.concordia.ca/auto/). The code for regenerating the figures is available online [2].
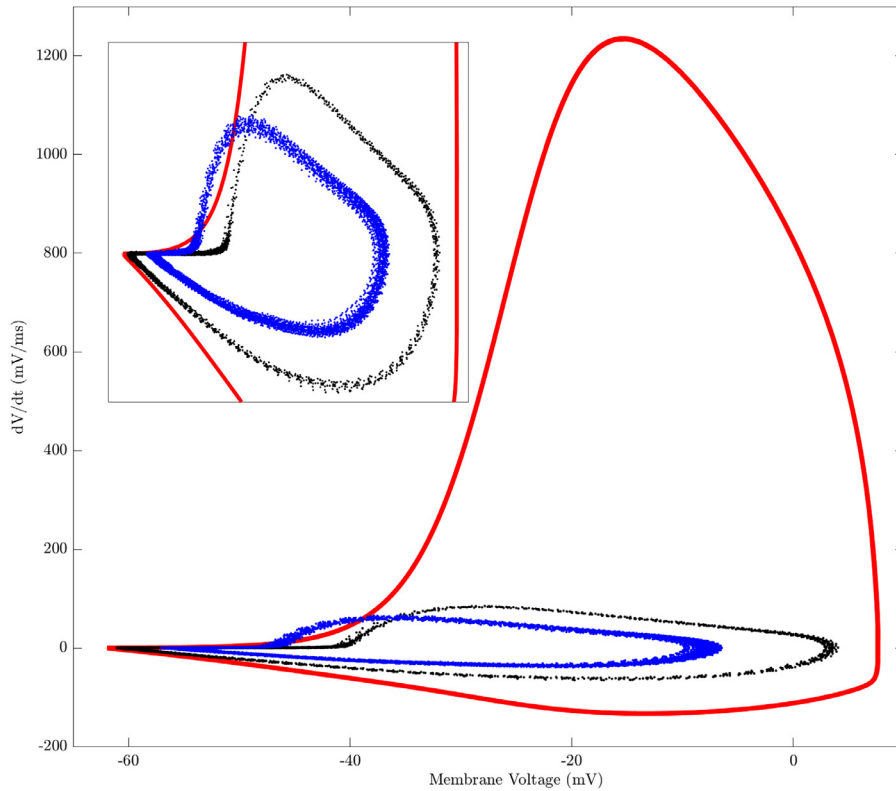
Fig. 1. The pre- and post-runup AP-cycles obtained experimentally differ significantly from those generated by the original model developed in [5,23]. The AP-cycles generated by the model (red), with its original parameters, has very few common features with the pre-runup (black) and post-runup (blue) AP-cycles obtained experimentally when plotted in the $(V, dV/dt)$-plane. Inset shows magnified plots of the cycles in the same $(V, dV/dt)$-plane. (For interpretation of the references to colour in this figure legend, the reader is referred to the web version of this article.)

Table 1
Parameter values of the ionic currents included in Eq. (1). Whenever two values are provided for a single parameter, the first corresponds to pre-runup ($t = 0$ min) while the second (between parentheses) corresponds to post-runup ($t = 25$ min).

	g_η (μS/cm^2)	E_η (mV)	Activation			Inactivation		
			v_x (mV)	s_x (mV)	τ_x (ms)	v_x (mV)	s_x (mV)	τ_x (ms)
I_{Na}	3.4	+55	−37 (−44)	+3	–	−40 (−48.5)	−4	$\tau_h(V)$
I_K	9.0556	−80	−23	+5	$\tau_n(V)$	–	–	–
I_L	0.07407	−38	–	–	–	–	–	–
I_A	15.0159	−80	−27 (−41)	+13.2	5	−80 (−96)	−6.5 (−9.2)	10
I_T	0.45045	+22	−50	+3	–	−68	−3.75	15

Table 2
The values of the other parameters appearing in the model described by Eqs. (1)–(2).

Parameter	Value	Parameter	Value
C_m	15.0148 μF/cm^2	y_0	0.1 ms
A	322 ms.mV	w	46 mV
V_c	-74 mV	–	–

3. Results

3.1. Bifurcation structure: quiescence and tonic firing

In [23], it was shown experimentally that cerebellar stellate cells exhibit type I excitability, demonstrated by generating a frequency-current plot in which arbitrarily low tonic spiking frequency could be achieved. This suggests that the revised
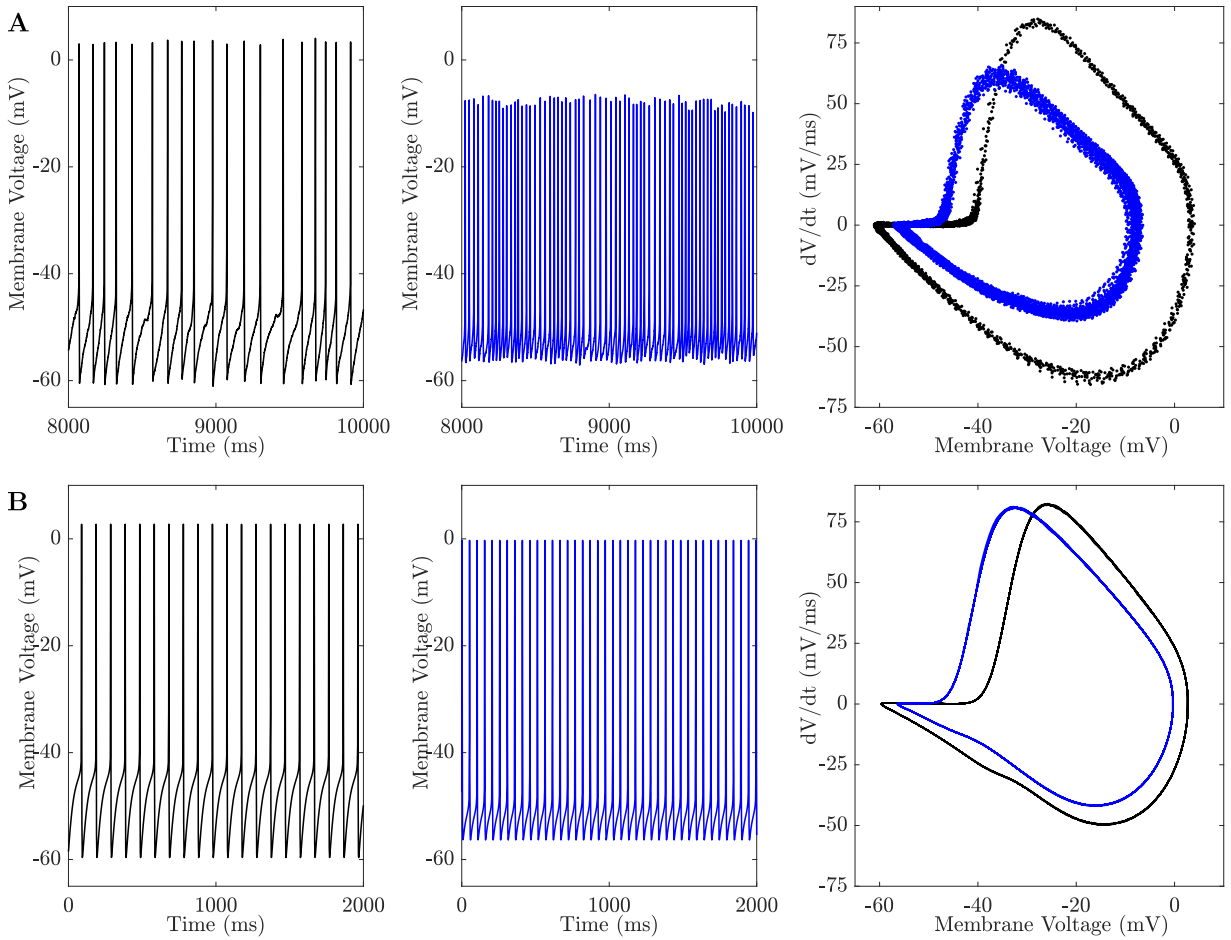
Fig. 2. Data fitting based on spike frequency and cycle shape of the AP. A comparison of experimental data and model simulations during pre- and post-runup. **A**) Experimental data of a tonically spiking stellate cell shown as time series during pre- (left) and post-runup (middle), and as cycles (right) in the $(V, dV/dt)$-plane. Black: pre-runup; blue: post-runup. **B**) Simulations of a tonically spiking stellate cell shown as time series during pre- (left) and post-runup (middle), and as cycles (right) in the $(V, dV/dt)$-plane. Black: pre-runup; blue: post-runup. Data fitting is based on matching the frequency and profile of the cycle during pre-runup, followed by capturing the dynamics of post-runup by varying only the steady-state (in)activation curves. (For interpretation of the references to colour in this figure legend, the reader is referred to the web version of this article.)

ionic model, given by Eqs. (1)–(2) (see Methods Section), must possess a bifurcation structure consistent with that of type I oscillators.

To confirm this, we plot in Fig. 3**A** the bifurcation diagram of membrane voltage V with respect to the applied current I_{app} during both pre-runup at $t = 0$ min (light colors) and post-runup at $t = 25$ min (dark colors). In both cases, we obtain bifurcation diagrams that exhibit two branches of stable nodes (blue-solid lines) and saddle fixed points (red-dashed lines) that meet at a saddle-node bifurcation. They also possess envelopes of stable limit cycles (green solid lines), representing the max/min V-values of the limit cycles, that terminate at homoclinic bifurcations coinciding with the saddle-node bifurcations. In other words, according to model (1)–(2), the transition from quiescence to spiking occurs through a saddle node on an invariant cycle (SNIC) bifurcation (see Fig. 4), a hallmark of type I excitability.

As suggested by the model, changes in the kinetics of I_{Na}, I_K and I_A during runup results in a leftward shift in the SNIC bifurcation along with a downward shift in both the fold of fixed points and the envelope of limit cycles. The SNIC bifurcation during post-runup (dark colors) occurs at a more negative value of I_{app} which gives rise to a higher frequency of spontaneous firing compared to pre-runup (light colors) when $I_{app} = 0$ pA. This is reflected in Fig. 3**B**, showing that the curves of limit-cycle periods (i.e., the interspike interval) become infinite towards the SNIC for both pre- (gray) and post-runup (black). The latter, however, lies below the former at $I_{app} = 0$ pA, indicating that runup increases the firing frequency at $I_{app} = 0$ pA. In addition, the leftward shift of the SNIC bifurcation during runup shown in Fig. 3**A** reflects a lower rheobase value, while its downward shift indicates a lower voltage threshold.

As a result of the decreased rheobase and firing threshold, the model is able to capture the experimentally recorded voltage-time traces produced by cerebellar stellate cells when current-step and ramp protocols are applied [3]. In what follows, we establish how the ghost of the SNIC affects the latency to first spike during pre- and post-runup.
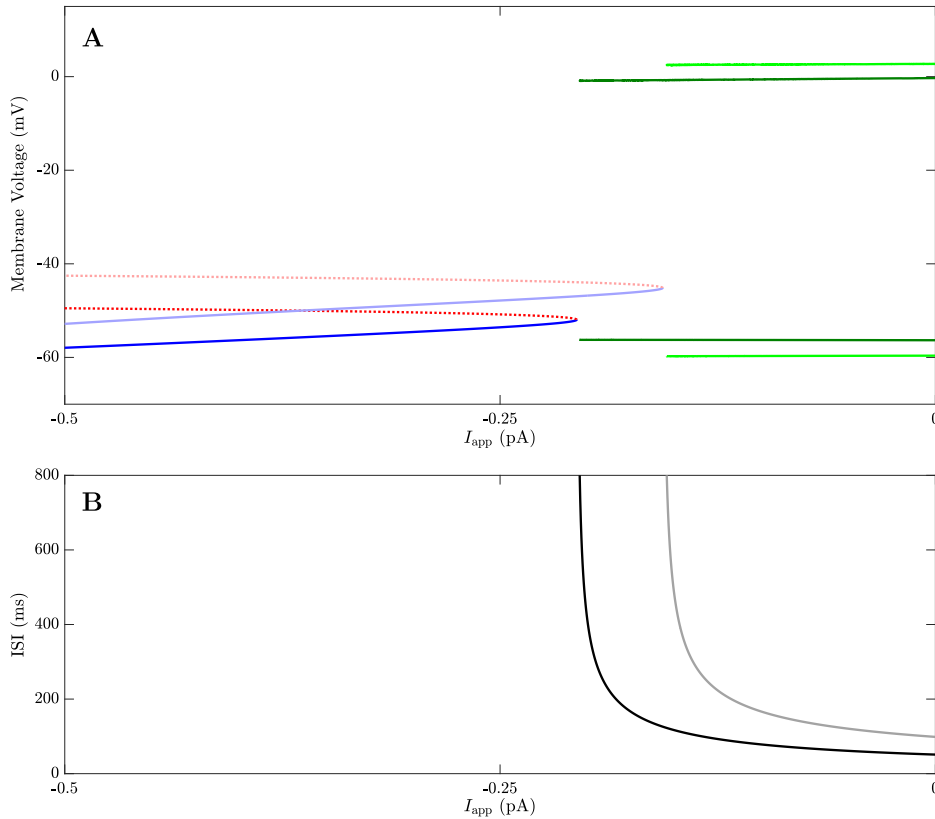
Fig. 3. Bifurcation diagrams, showing the shifts in firing threshold, rheobase and frequency between pre- and post-runup. **A**) Bifurcation diagram of the membrane voltage (V) with respect to the applied current (I_{app}). A lower branch of stable nodes (blue-solid lines) and upper branch of unstable saddle fixed points (red-dashed lines) meet at a saddle-node bifurcation. Upper and lower envelopes of stable limit cycles (green-solid lines) originate from a Hopf bifurcation (not shown as it lies outside the region of interest) and terminate at a SNIC bifurcation. Light colors correspond to pre-runup ($t = 0$ min), while dark colors correspond to post-runup ($t = 25$ min). **B**) Interspike interval (period) of stable limit cycles corresponding to the green envelope shown in **A** during pre-runup (gray line) and post-runup (black line). (For interpretation of the references to colour in this figure legend, the reader is referred to the web version of this article.)

3.2. Non-monotonic latency profile of cerebellar stellate cells in pre- and post-runup

Applying a current-step protocol (similar to that shown in Fig. 5**A**) is quite common in patch-clamp experiments. The protocol consists of two parts, a hyperpolarizing bias-current (I_{bias}) during the step that silences the cell and an ensuing test-current (I_{test}) during the step that brings the membrane voltage of the cell above its firing threshold. The resting membrane voltage obtained by the application of I_{bias} will be referred to hereafter as the holding potential. Thus for every I_{bias}, a new holding potential is generated, each of which represents a given initial condition (IC). Using current-clamp experiments, it was shown in [23] that the latency to first spike in cerebellar stellate cells, evoked by such a protocol, exhibits a non-monotonic profile when plotted as a function of holding potentials (a peculiar outcome compared to other neuronal cell lines). The A-type K$^+$ and T-type Ca^{2+} channels were identified as the key players in generating this non-monotonic profile.

To check if first-spike latency differs between pre- and post-runup, we apply a step-current to the revised model, given by Eqs. (1)–(2), consisting of the same $I_{bias} = -0.21$ pA and differing $I_{test} = -0.15$ pA (pre-runup) and -0.2 pA (post-runup). Applying I_{bias} brings the system to the lower branch of Fig. 3, and sets it at a stable steady state representing a holding potential of the cell and the IC of the trajectory induced by the application of I_{test}. As shown in Fig. 6**A**, the latency to first spike appears shorter in duration for post-runup (blue) compared to pre-runup (black), further demonstrating that stellate cells become more excitable.

Further analysis of the revised model also reveals that we can produce non-monotonic first-spike latency profiles. This is demonstrated in Fig. 6**B**, showing that for pre- and post-runup, the latency of APs generated by injecting a step-current to the model, consisting of $I_{bias} = [-4.88, -0.16]$ pA and $I_{test} = -0.15$ pA for pre-runup and $I_{bias} = [-5.08, -0.21]$ pA and $I_{test} = -0.2$ pA for post-runup. In this figure, the magnitude of latency to first spike for each step-current is plotted as a function of the holding potential for pre- (black) and post-runup (blue). In both cases, the model produces initially a minor-to-moderate decrease in latency at low holding potentials (but less pronounced during pre-runup compared to post-runup) followed by a prominent non-monotonic component consisting of a pair of increasing and decreasing phases at higher holding potentials.
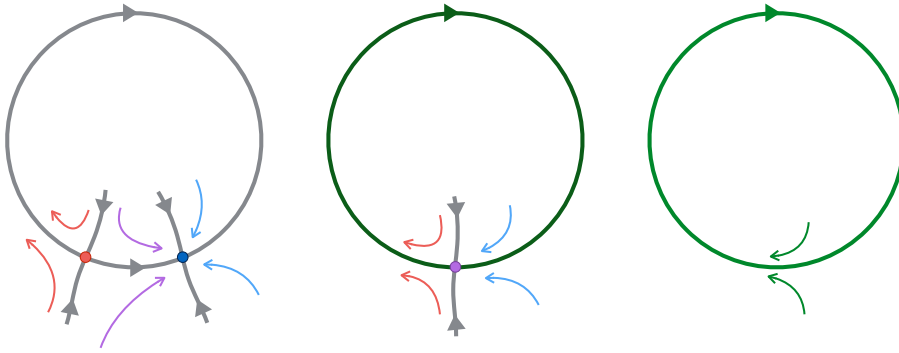
Fig. 4. Schematic diagram illustrating the dynamics near a saddle-node on invariant cycle (SNIC) bifurcation in phase-space. In the left panel, which corresponds to $I_{app} < I_{SNIC}$, the unstable invariant manifold (gray line) of the saddle fixed point (red dot) merges with the stable manifold (also gray line) of the stable node (blue dot). When $I_{app} = I_{SNIC}$ (middle panel), the saddle fixed point merges with the node (purple dot), generating a homoclinic orbit (dark-green circle). For $I_{app} > I_{SNIC}$ (left panel), the fixed points disappear and a limit cycle (light-green circle) persists. In all panels, arrows indicate the flow of solution trajectories. (For interpretation of the references to colour in this figure legend, the reader is referred to the web version of this article.)
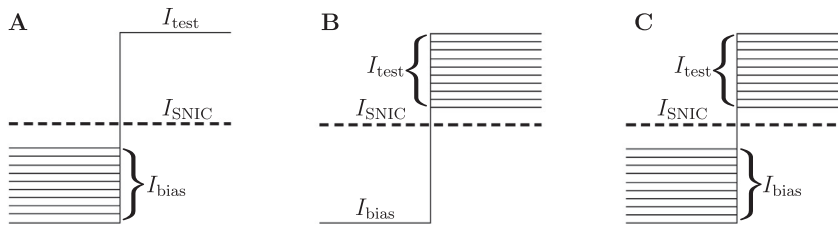

Fig. 5. Three variations of current-clamp (or current-step) protocols consisting of hyperpolarizing (bias) and depolarizing (test) currents applied to Eqs. (1)–(2). **A**) Current-clamp protocol consisting of varying hyperpolarization bias-currents (that each ensures quiescence) followed by a suprathreshold depolarization test-current. **B**) Current-clamp protocol consisting of a hyperpolarization bias-current followed by varying suprathreshold depolarization test-currents. **C**) Current-clamp protocol that combines the two protocols in **A** and **B**.

The increase in latency in the non-monotonic component of the pre-runup profile is more pronounced than that observed within the post-runup profile. In [23], the increase in latency obtained by the model (developed based on experimental conditions consistent with post-runup) was at most 60%, which is lower than that obtained by the model presented here during post-runup. We will demonstrate later that it is in fact possible to obtain arbitrarily large increases in first-spike latencies during pre- and post-runup starting from specific holding potentials.

These results thus show that the revised model, given by Eqs. (1)–(2) does generate non-monotonic latency profiles in agreement with experimental recordings. Note that we have chosen $I_{app} = I_{test}$ for pre- and post-runup that form the same distance from I_{SNIC} for each case; the corresponding holding potentials for I_{SNIC} are indicated by vertical dashed lines in Fig. 6**B**.

3.3. Ghost of the SNIC and slow regions

In order to understand why first-spike latencies, produced by the model described in Eqs. (1)–(2), exhibit non-monotonic profiles, we first need to quantify the L_2-norm of the vector field **F**, given by

$$\|\mathbf{F}\|_2 = \left\| \left(\frac{dV}{dt}, \frac{dh}{dt}, \frac{dn}{dt}, \frac{dn_A}{dt}, \frac{dh_A}{dt}, \frac{dh_T}{dt} \right) \right\|_2,$$

along transient solution trajectories that start from initial conditions near the attractor, i.e., the limit cycle. Recall that upon the application of the hyperpolarizing current $I_{app} = I_{bias}$, membrane potential is set at a steady state that lies on the lower stable branch of Fig. 3**A**. This means that when the suprathreshold depolarizing current I_{test} is applied, the trajectory will be initiated from that steady state, acting as an IC for this trajectory that propagates towards the limit cycle corresponding to $I_{app} = I_{test}$. The magnitude of $\|\mathbf{F}\|_2$ thus describes how fast solution trajectories corresponding to various I_{bias} evolve within phase space. By color-coding them based on the magnitude of $\|\mathbf{F}\|_2$, we can determine if there are slow regions within the phase space that may alter latencies. By applying the same current-step protocol as the one used in Fig. 6**B**, for the post-runup model, and by projecting the resulting trajectories onto the (V, h_A, h_T)-space as in Fig. 7**A** reveals that indeed, for $I_{bias} = [-5.08, -0.21]$ pA and $I_{test} = -0.2$ pA, we observe a slow region (blue area) near the top-right of the limit cycle (black) through which these trajectories pass. This slow region is a manifestation of how close the system is to a SNIC bifurcation in parameter space. This was previously referred to as the ghost of the SNIC in a two dimensional phenomenological model
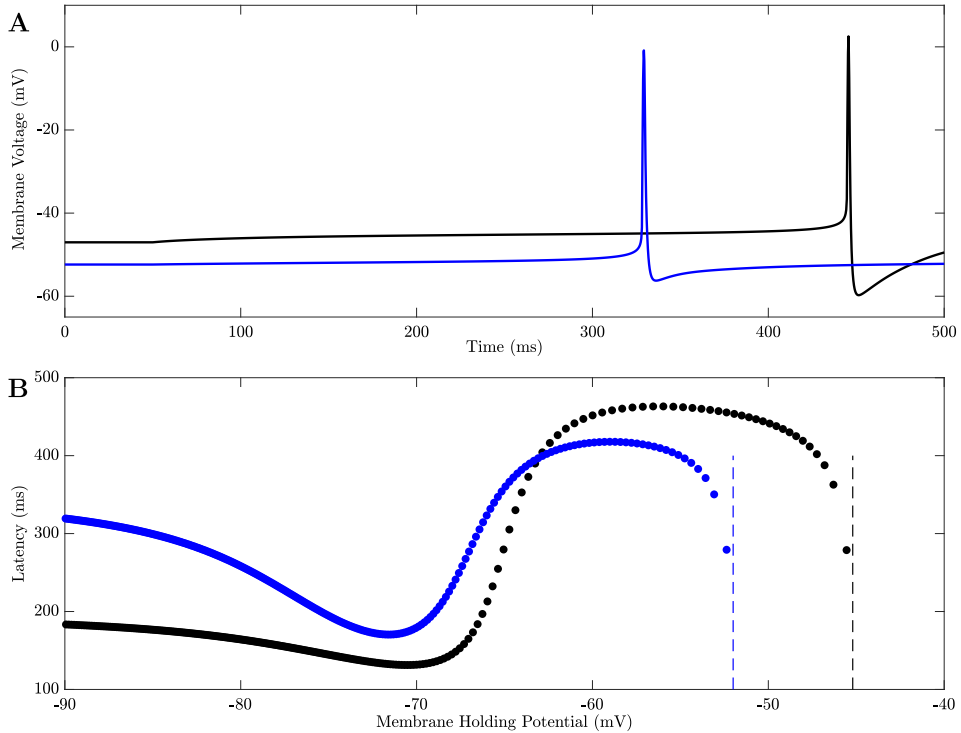
Fig. 6. Non-monotonic profiles of first-spike latency in relation to the membrane holding potential during both pre- and post-runup. **A**) APs generated by the model given by Eqs. (1)–(2) in response to a step-current with the same $I_{bias} = -0.21$ pA, but $I_{test} = -0.15$ pA for pre-runup (black line) and $I_{test} = -0.2$ pA for post-runup (blue line) **B**) Magnitude of first-spike latencies of all these APs plotted as a function of the membrane holding potential for pre-runup (black line) and post-runup (blue line). For pre-runup: $I_{bias} = [-4.88, -0.16]$ and $I_{test} = -0.15$ pA; for post-runup: $I_{bias} = [-5.08, -0.21]$ and $I_{test} = -0.2$ pA. Vertical dashed lines correspond to holding potentials for I_{SNIC}. Notice the rise and decline in latency at high values of holding potential, indicating a non-monotonic first-spike latency in both pre- and post-runup. (For interpretation of the references to colour in this figure legend, the reader is referred to the web version of this article.)

in [15], and the passage time within this slow region was quantified to be proportional to $1/\sqrt{|I_{app} - I_{SNIC}|}$, where I_{SNIC} and I_{app} are the magnitudes of the depolarizing step-currents (test-currents) landing at the SNIC and beyond, respectively.

Fig. 7**A** thus shows that the latency to first spike in the stellate cell model not only depends on the size of the slow region and how slowly solution trajectories evolve therein, but also on how far ICs are from the attractor. Solution trajectories that start near the limit cycle end up passing through the slow region and take a moderate amount of time to reach the attractor, making latencies relatively short. Solution trajectories that start slightly further away from the limit cycle still pass through the slow region while also having to travel further in order to reach it, creating longer latencies. However, those solution trajectories that start relatively far from the attractor end up bypassing the slow region, and so even though they must travel a greater distance, they evolve towards the limit cycle considerably faster, resulting in shorter latencies. As a result, latencies to first spike end up exhibiting a non-monotonic profile during an increase in membrane holding potential, as seen in Fig. 6**B**.

3.4. Infinite latencies in pre- and post-runup

We have so far shown that the distance from the attractor along with the slow region dictate how long the latency to first spike is in the current-step protocol of Fig. 5**A**. In order to determine how these non-monotonic latency profiles change while modifying the magnitude of I_{test}, we have plotted in Fig. 7**B** the three-dimensional graphs of these profiles as a function of the holding potential and I_{test} (see Fig. 5**C**) for both pre-runup (top), when $I_{bias} = [-4.88, -0.16]$ pA, and post-runup (bottom), when $I_{bias} = [-5.08, -0.21]$ pA. For both pre- and post-runup, I_{test} varies between 1 pA and I_{SNIC}, the associated applied current when the system undergoes a SNIC bifurcation. Overall, these latency profiles maintain their non-monotonic nature, but appear in the pre-runup case to make latencies arbitrarily large only for one component of the profile (labeled segment (C) in Fig. 8**A** (top)) as $I_{test} \longrightarrow I_{SNIC}^{+}$. Indeed, Fig. 8**A** (bottom) shows that the line $I_{test} = I_{SNIC}$ is a vertical asymptote for the latencies in segment (C), but not so for segments (A) and (B) which appear to show finite latencies close to the SNIC bifurcation. We will see later that the boundaries of segments (A), (B) and (C) can be more precisely defined based on the stable manifold of the saddle points and saddle nodes.
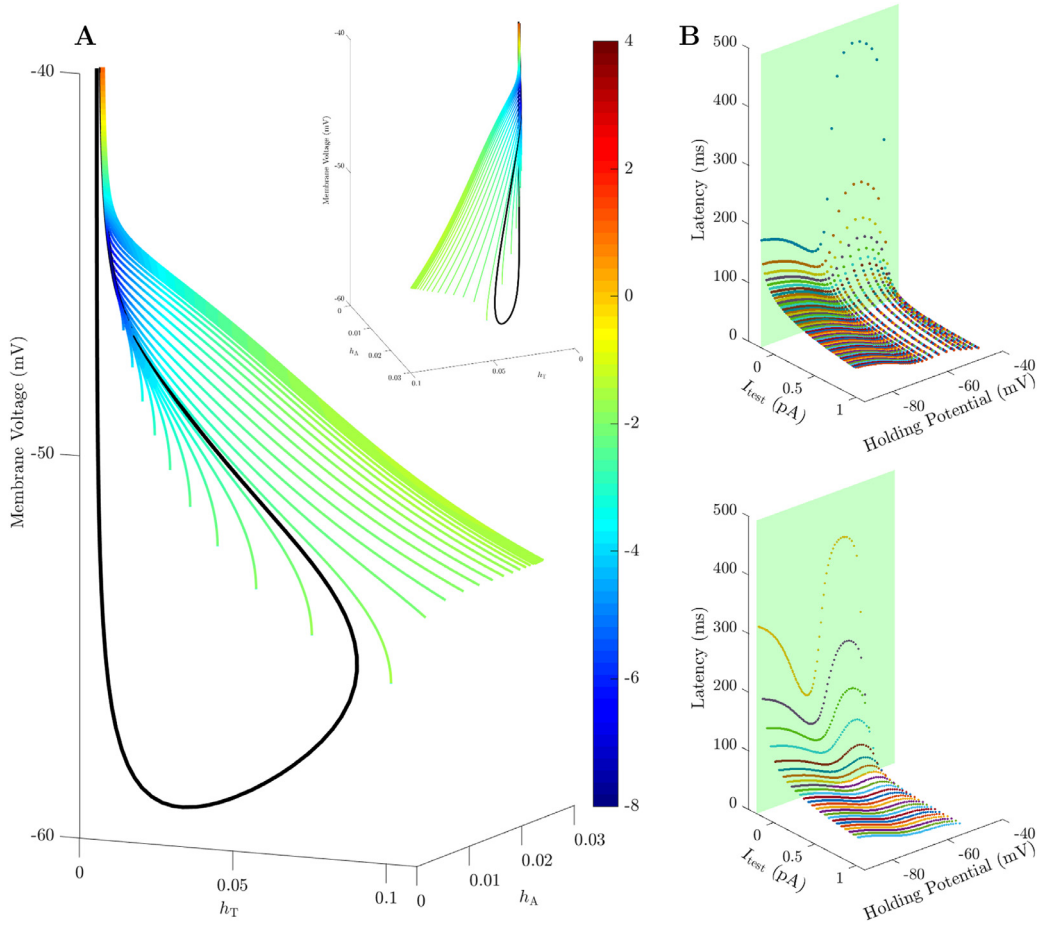
Fig. 7. Distance from the stable limit cycle (attractor) along with the slow region (ghost of the SNIC) produce non-monotonic latency profiles in pre- and post-runup. **A**) Solution trajectories starting from different ICs, projected onto the (V, h_A, h_T)-space, approach the attractor during post-runup. They are color-coded based on their speeds (magnitude of $\|\mathbf{F}\|_2$) indicated in the color-bar in logarithmic scale on the right. The inset shows the same set of trajectories viewed from a different angle. **B**) Latency profiles for pre-runup (top) and post-runup (bottom) obtained using current-step protocols similar to Fig. 5**C**. Each profile is plotted as a function of holding potential (determined by I_{bias}) generated by applying a suprathreshold depolarizing step-current (I_{test}). For each specific I_{test} in the current-step protocol, a new profile is generated. For pre-runup: $I_{bias} = [-4.88, -0.16]$ pA and $I_{test} = [1, I_{SNIC}]$ pA; for post-runup: $I_{bias} = [-5.08, -0.21]$ pA and $I_{test} = [1, I_{SNIC}]$ pA.

These finite/infinite latencies seen in the pre-runup profiles are not completely retained in the post-runup profiles (see Fig. 7**B** (bottom)). In this latter case, we only observe finite latency for segment (B) (defined by Fig. 8**B** (top)), and arbitrarily large latencies for segments (A) and (C) as $I_{test} \longrightarrow I_{SNIC}^+$. We verified these results in Fig. 8**B** (bottom) by showing that the line $I_{test} = I_{SNIC}$ acts as a vertical asymptote for latencies in segments (A) and (C).

These results demonstrate that the slow region associated with the ghost of the SNIC persists for both pre- and post-runup for any depolarizing $I_{test} \geq I_{SNIC}$ in the current-step protocol, and that the magnitude of these latencies could be made arbitrarily large for certain segments of the profiles as $I_{app} \longrightarrow I_{SNIC}^+$. In the following, we will illustrate how the topology of the SNIC (depicted in Fig. 9) governs which segment of the latency profile becomes unbounded in the limit when $I_{test} \longrightarrow I_{SNIC}^+$.

3.5. Holding membrane potential and the topology of the SNIC determine if latencies are bounded or not

During the current-step protocol of Fig. 5**C**, a number of hyperpolarizing bias-currents, given by I_{bias}, are applied to the stellate model to hold the membrane potential at various voltages. In other words, each I_{bias} specifies the ICs of the solution trajectory of the model (representing the spiking membrane voltage) triggered by a depolarizing step-current (test-current) given by I_{test}. For $I_{test} \gg I_{SNIC}$, the test-current is suprathreshold, resulting in solution trajectories that oscillate rhythmically (i.e., spike periodically) around the limit cycles (see Fig. 9 (right)). The slow region in this case is small and few trajectories will pass through it. When I_{test} is only marginally bigger than I_{SNIC}, then the slow region is larger and solution trajectories are more likely to pass throughout it, making their first-spike latencies longer (Fig. 9 (middle)).
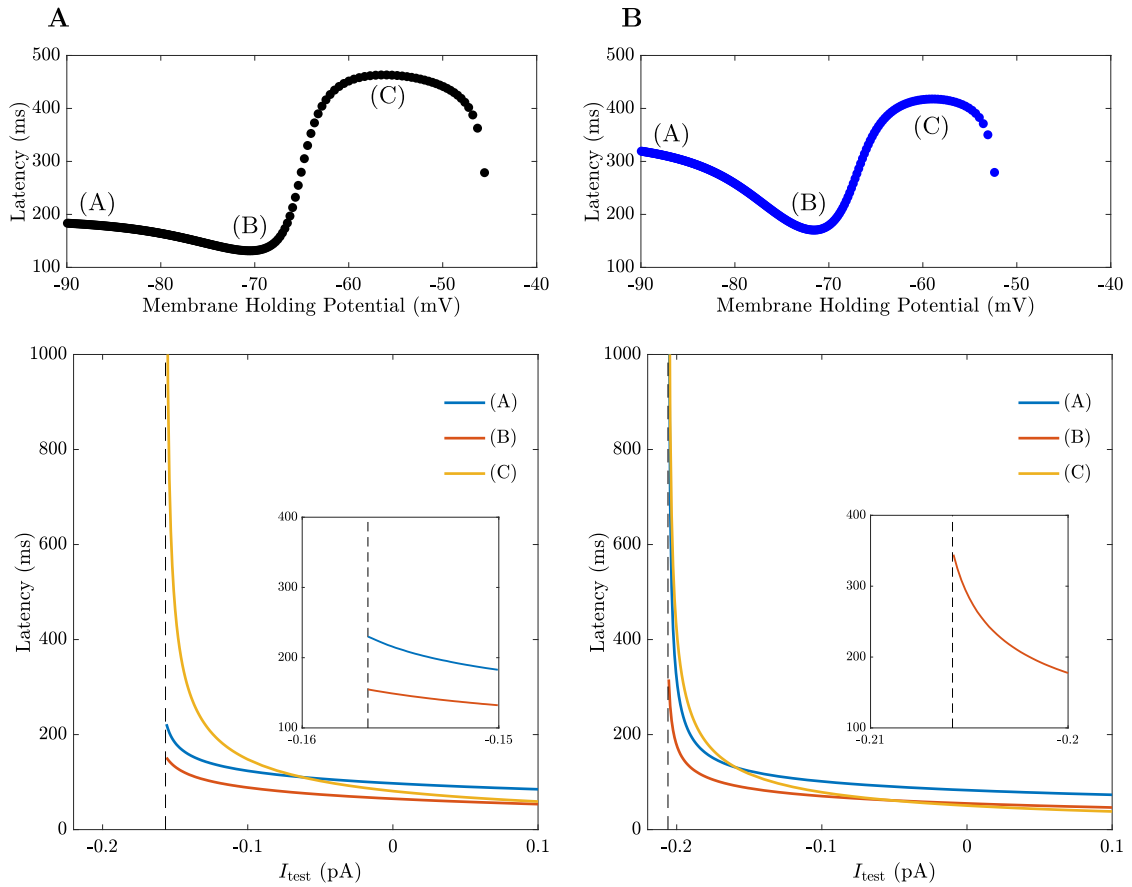
Fig. 8. Infinite first-spike latencies generated when $I_{\text{test}} \longrightarrow I_{\text{SNIC}}^{+}$. **A**) One segment of the non-monotonic latency profile, namely (C), associated with pre-runup (top) asymptotically grow to infinity along the vertical dashed line (defined by $I_{\text{test}} = I_{\text{SNIC}}$) as $I_{\text{test}} \longrightarrow I_{\text{SNIC}}^{+}$ (bottom). The three segments in the top panel are labeled (A), (B) and (C) and color-coded based on the legend displayed in the bottom panel. **B**) The two segments (A) and (C) (top) of the non-monotonic latency profile associated with post-runup, asymptotically grow to infinity along the vertical dashed line (defined by $I_{\text{test}} = I_{\text{SNIC}}$) as $I_{\text{test}} \longrightarrow I_{\text{SNIC}}^{+}$ (bottom). Each segment is color-coded based on the legend displayed in the bottom panel. Insets in the bottom panels show the magnified portions of the latency curves that correspond to the segments with finite latency near the SNIC.
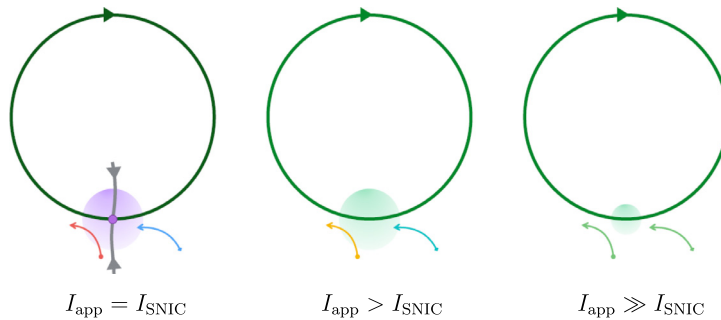

Fig. 9. Schematic diagram illustrating how the topology of the SNIC and the slow region affects latency. Left panel ($I_{\text{app}} = I_{\text{SNIC}}$): The stable invariant manifold (gray line) of the saddle node (purple dot) divides solution trajectories into two groups: those that start with initial conditions to the left of the stable invariant manifold and transiently follow the homoclinic orbit (dark-green circle), each generating a single transient spike, and those that start with initial conditions to the right of the stable invariant manifold and never spike, gradually approaching the saddle node. Solution trajectories that pass through the slow region surrounding the saddle node (purple shaded area) will slow down. Middle panel ($I_{\text{app}} > I_{\text{SNIC}}$): The saddle node disappears and the homoclinic orbit turns into a stable limit cycle. The two groups of solution trajectories, identified in the left panel, both spike tonically in this configuration while approaching the limit cycle. Those that pass through the slow region (green shaded area) will slow down, causing long first-spike latencies. Right panel ($I_{\text{app}} \gg I_{\text{SNIC}}$): Similar to middle panel except that the slow region (green shaded area) is smaller. In all panels, arrows indicate the flow of solution trajectories. (For interpretation of the references to colour in this figure legend, the reader is referred to the web version of this article.)

In the limit when $I_{\text{test}} \longrightarrow I_{\text{SNIC}}^+$, however, the system gradually approaches the topology of a SNIC bifurcation, consisting of a saddle node and a homoclinic orbit (Fig. 9 (right)). The initial conditions of these solution trajectories become the key determinant of how they will behave at steady state. If the initial conditions are located to the left of the stable invariant manifold of the saddle node, then in the limit as $I_{\text{test}} \longrightarrow I_{\text{SNIC}}^+$, solutions will evolve towards the periodic orbit (and may pass through the slow region) generating oscillations with different but bounded first-spike latencies. In contrast, if the ICs are located to the right of the stable invariant manifold of the saddle node, then in the limit as $I_{\text{test}} \longrightarrow I_{\text{SNIC}}^+$, solutions will transition from being oscillatory to non-oscillatory, gradually propagating towards the saddle node which produces infinite latencies.

In the pre-runup case, the ICs of solution trajectories associated with segments (A) and (B) in Fig. 8**A** (top) lie to the left of the stable invariant manifold of the saddle node highlighted in Fig. 9 (left) whereas in the post-runup case, only ICs of solution trajectories corresponding to segment (B) of Fig. 8**B** (top) lie to the left of the stable invariant manifold of the saddle node, producing finite latencies. In other words, ICs that lie to the right of the stable invariant manifold of the saddle node, produce latencies that become infinite when $I_{\text{test}} \to I_{\text{SNIC}}^+$, as is the case for segment (C) during pre-runup and segments (A) and (C) during post-runup. That explains why some segments of the non-monotonic latency profiles of Fig. 8 (top) approach infinity as $I_{\text{test}} \longrightarrow I_{\text{SNIC}}^+$.

3.6. Transient single spiking evoked by sub-threshold step-currents

The above results, along with Fig. 9 (left), indicate that it is possible for solution trajectories to produce transient single spikes associated with the SNIC for "sub-threshold" step-currents $I_{\text{test}} < I_{\text{SNIC}}$ provided that the ICs (or membrane holding potentials determined by the magnitude of I_{bias} in the current-step protocol) of solution trajectories lie to the left of the stable manifold of the saddle node. Since in the pre-runup case, ICs lie to the left of the stable invariant manifold of the saddle node for strongly hyperpolarized holding potentials corresponding to segments (A) and (B) in Fig. 8**A**, transient single spikes can be generated by the stellate cell model in this case. For the post-runup case, however, transient single spikes occur only for a limited interval of holding potentials in the intermediate range (corresponding to segments (B) in Fig. 8**B**). Such transient spiking behavior is different from those previously seen in [22,28].

For a given pair of I_{bias} and I_{test}, one can find the boundary between the transient single spiking regime and tonic spiking regime in the $(I_{\text{bias}}, I_{\text{test}})$-plane during pre-runup. As one would expect, this boundary is given by the vertical line $I_{\text{test}} = I_{\text{SNIC}}$. Color-coding these regimes based on the magnitude of first-spike latencies generates the heat-map shown in Fig. 11. In that heat-map, the vertical dotted line represents the boundary $I_{\text{test}} = I_{\text{SNIC}}$ separating the two main regimes: the tonically spiking regime to the right of the vertical dotted line, and the transiently spiking (blue)/quiescent (burgundy) regime to the left. Quiescent activities produce infinite latencies, which explains the dark burgundy color. As discussed before, the boundary between no activities (quiescence) and single spiking activities to the left of the vertical dotted line $I_{\text{test}} = I_{\text{SNIC}}$ and below the white arrow is determined by where the ICs (or the holding potentials specified by I_{bias}) lie relative to the stable invariant manifold of the saddle (SIMS). For $I_{\text{test}} = I_{\text{SIMS}}$, the IC lies exactly on the SIMS producing infinite latency. This indicates that latencies associated with transient single spikes will increase to infinity as $I_{\text{test}} \longrightarrow I_{\text{SIMS}}^+$. Interestingly, the width of the single spiking regime below the white arrow changes and is maximal for $I_{\text{bias}} \approx -1.5 \, \text{pA}$. Above the white arrow, on the other hand, single spiking disappears and the stable invariant manifold of the saddle node becomes the boundary between regimes of tonic spiking and quiescence. Right at the tip of the white arrow, SIMS is replaced by the stable manifold of the saddle node.

In the post-runup case (see Fig. 11**A**), the heat-map of first-spike latency shows that the single spike activity region to the left of the vertical line $I_{\text{test}} = I_{\text{SNIC}}$ is smaller in range to that seen in the post-runup case. More specifically, for I_{test} very close to I_{SNIC} and I_{bias} between the white arrows, SIMS always separates the single spiking regime to the right from the quiescent (infinite latency) regime to the left.

The results obtained in Fig. 11**A** now allow us to precisely define the boundaries of segments (A), (B) and (C) of Fig. 8**B** (for post-runup), defined loosely in Section 3.4. Specifically, segment (B) lies between the two white arrows in Fig. 11**A**, while segments (A) and (C) lie below the bottom arrow and above the upper arrow, respectively. As indicated by Figs. 8**A** and 10, the same idea can be extended to the pre-runup case to precisely define the boundaries of the various segments. In this latter case, segments (A) and (B) form one merged segment that is separated from segment (C) at the tip of the white arrow.

The level sets of the heat-map in Fig. 11**A**, obtained by taking the set of all pairs $(I_{\text{test}}, I_{\text{bias}})$ that possess the same first-spike latency, produce level curves (solid lines) that, when projected onto the $(I_{\text{test}}, I_{\text{bias}})$-plane, are tangential to the horizontal line $I_{\text{bias}} = I_{\text{SNIC}}$ (see Fig. 11**B**). Extending these level curves (dashed lines) generate a fold (see inset in Fig. 11**B**) that corresponds to the same fold seen at the saddle node bifurcation in Fig. 3. In other words, the dashed portion of the level curves to the left of the tangential points represent first-spike latencies that start from holding potentials lying on the saddle fixed points of Fig. 3 (rather than from those holding potentials determined by the stable nodes). Note that the level curves appear to intersect each other (see inset), even though they do not, due to the fact that they are projected onto the $(I_{\text{test}}, I_{\text{bias}})$-plane. As seen in the inset, the latencies gradually approach infinity as the level curves approach the line $I_{\text{bias}} = I_{\text{test}}$, which represents the case when no step-current is applied.
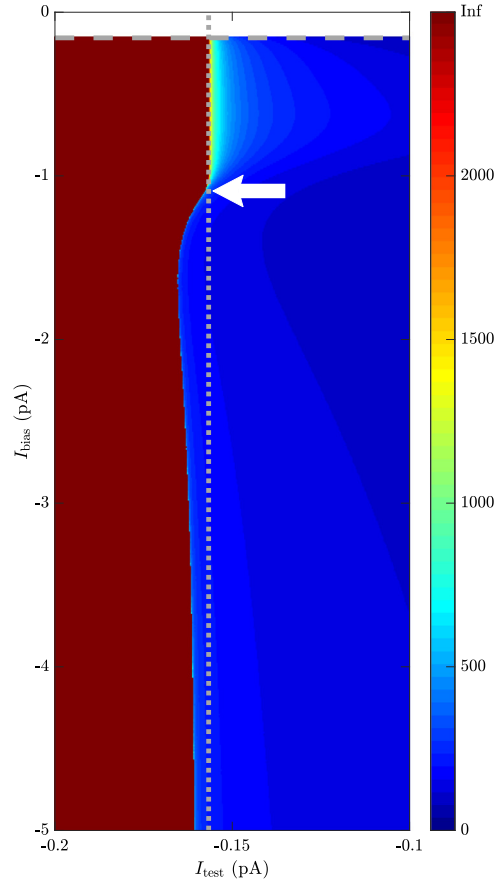
Fig. 10. First-spike latencies associated with transient single and tonic spiking activities during pre-runup. Heat-map showing the regimes of excitability during pre-runup, color coded based on the magnitude of the first-spike latencies ranging from infinite (burgundy) to small (blue) as defined by the color-bar shown on the right. The horizontal (vertical) dashed (dotted) line represents the location of the SNIC relative to the bias-current (test-current), i.e., when $I_{\mathrm{bias}} = I_{\mathrm{SNIC}}$ ($I_{\mathrm{test}} = I_{\mathrm{SNIC}}$). To the right of the vertical dashed line, we obtain tonic spiking activities while to the left, we observe quiescence (burgundy) or single transient spike (blue) for I_{bias} below the white arrow. (For interpretation of the references to colour in this figure legend, the reader is referred to the web version of this article.)

3.7. Firing "threshold" during synaptic (dynamic) inputs

It was shown in [23], that when stellate cells are subjected to a pair of inhibitory and excitatory post-synaptic (dynamic) inputs, labeled IPSI and EPSI, respectively, separated by a time period of 15 ms, they exhibit very peculiar responses; they fire APs in response to an EPSI when the conductance of the preceding IPSI is either zero or large enough, but do not do so for intermediate IPSI conductances [23]. There, the authors verified these results using their stellate cell model by applying an input signal that combines the IPSI and EPSI, given by

$$I_{\mathrm{syn}}(t) = g_{\mathrm{exc}}(t - 15)\,V\,e^{-3(t-15)}\,H(t - 15) + g_{\mathrm{inh}}\,t\,e^{-1.25t}\,(V + 82), \tag{3}$$

where $H(t)$ is the Heaviside step function. These results appear to be ultra sensitive to small changes in the amplitude of EPSI conductance, g_{exc}.

To determine if the revised stellate cell model, described by Eqs. (1)–(2), is capable of producing similar but more robust switching behavior in responsiveness upon stimulation by a pair of IPSI and EPSI with varying amplitudes of IPSI, we devise a similar approach to that used in [23]. This is done by injecting an input signal, identical to the one used in Eq. (3), into the model during pre- and post-runup (see Fig. 12**A** and **B**, respectively). The amplitude of the EPSI conductance is kept fixed in both cases at $g_{\mathrm{exc}} = 3$ pS and 1.6 pS, respectively, but the amplitude of IPSI conductance is gradually increased from 0 pS (orange) to 1.5 pS (red) and then to 3 pS (green) during pre-runup, and from 0 pS (orange) to 1 pS (red) and then to 2 pS (green) during post-runup. As was the case in [23], the revised model produces AP for the first and third combinations of $(g_{\mathrm{inh}}, g_{\mathrm{exc}})$, but not the middle, for both cases (see 12**A** and **B**, respectively).

To examine the robustness of this switching behavior of the stellate cell model, an entire range of $g_{\mathrm{exc}} \in [0, 5]$ pS and $g_{\mathrm{inh}} \in [0, 5]$ pS is tested during pre-runup (Fig. 12**C**) and post-runup (Fig. 12**D**). Our results reveal that, in both cases, two regimes of behavior can be identified in the $(g_{\mathrm{inh}}, g_{\mathrm{exc}})$-parameter space: (i) a non-responsive regime (colored in yellow)
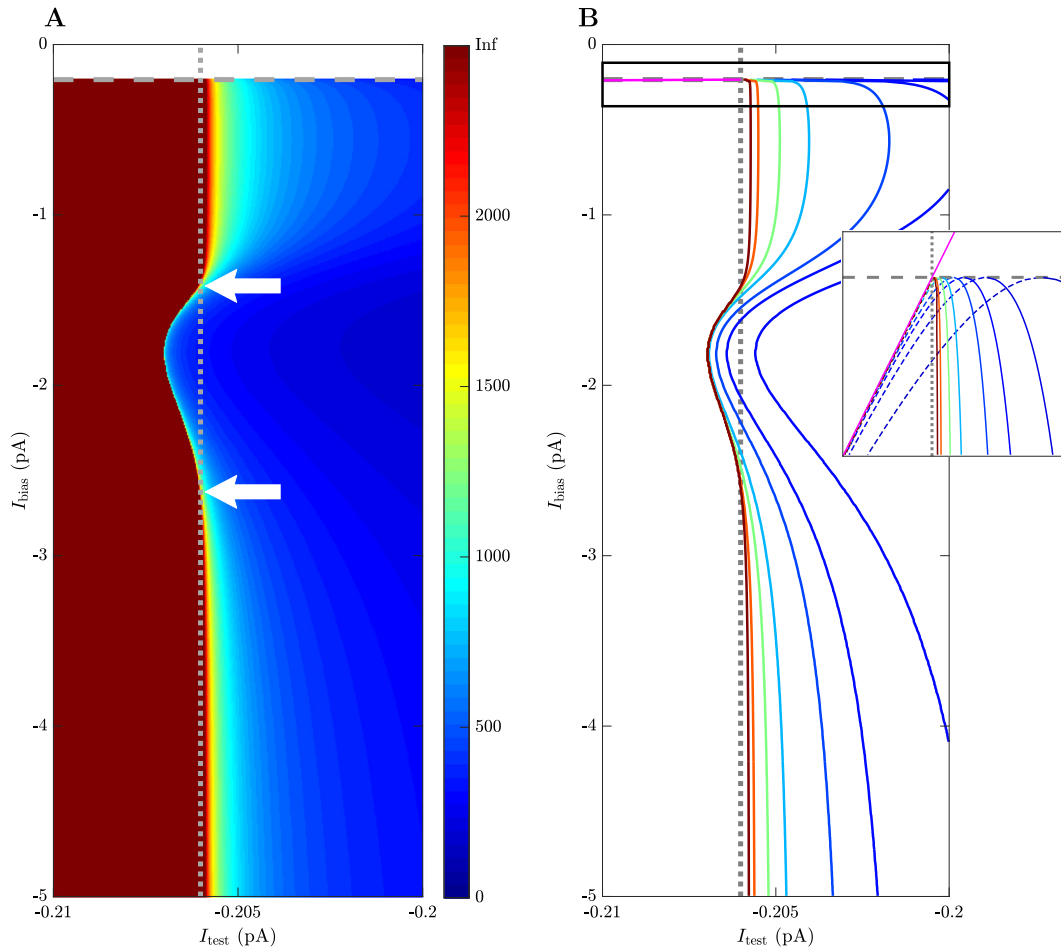
Fig. 11. First-spike latencies associated with different activity regimes during post-runup. **A**) Heat-map shows the regimes of excitability during post-runup, color coded based on the magnitude of first-spike latencies ranging from small (blue) to infinite (burgundy) as indicated by the color-bar on the left. The horizontal (vertical) dashed (dotted) line represents the location of the SNIC relative to the bias-current (test-current), i.e., when $I_{bias} = I_{SNIC}$ ($I_{test} = I_{SNIC}$). To the right of I_{SNIC}, we obtain tonic spiking activities, while to the left, we either observe quiescence (burgundy) or single spike activity (blue). White arrows also indicate where the stable invariant manifold of the saddle node turns into the stable invariant manifold of the saddle (SIMS) as a boundary for single spiking. **B**) Level curves of the heat-map in **A** (solid lines) projected onto (I_{bias}, I_{test})-plane. These level curves are further extended (dashed lines) to show the latencies of APs initiated from the saddle fixed points. These level curves are obtained by taking the set of all points (I_{bias}, I_{test}) that have the same first-spike latency: 300 ms, 400 ms, 500 ms, 750 ms, 1000 ms, 1500 ms and 2000 ms (blue to burgundy). The level curves are color-coded based on the magnitude of the latency as indicated by the color-bar in **A**. Inset shows the magnified portion of the level curves enclosed inside the rectangle in **B**. (For interpretation of the references to colour in this figure legend, the reader is referred to the web version of this article.)

that does not exhibit any spiking activity, and (ii) a responsive regime that exhibit spiking activity in response to such synaptic inputs. The responsive regimes in panels **C** and **D** are color-coded based on the duration of first-spike latency, which shows that these latencies gradually increase to infinity near the boundary between the responsive and non-responsive regimes. The orange, red and green dots in both of these two panels show that, during pre- and post-runup, the switching between the responsive and non-responsive regimes can occur twice within the interval $g_{exc} \in [2.06, 4.02]$ pS and $g_{exc} \in [1.56, 1.64]$ pS, respectively. Indeed, further increase in g_{inh} induces switching from spiking to quiescence again. When g_{exc} is small (near ~ 0 pS), however, the model can either generate no response (no triggered spiking), regardless of the amplitude of the inhibition, or only one switching from spiking to quiescence (near ~ 1.2 pS). These results thus indicate that, for sufficiently large EPSI conductance, switching between responsiveness and non-responsiveness in this model is robust, but more so during pre-runup than post-runup.

One interesting aspect of the simulations performed in Fig. 12**A** and **B** is that, although the middle combination of IPSI and EPSI does not trigger an AP in membrane voltage, it induces a plateau response that is higher in amplitude than the one generated by the third combination prior to spiking. In other words, the former combination IPSI and EPSI appears to surpass the firing threshold of the latter, but still fails to evoke an AP. The stable manifold of the saddle appears to be playing a key role in producing this type of behavior and in defining the boundary between the responsive and non-responsive regimes of Fig. 12**C** and **D**. This remains to be verified dynamically.
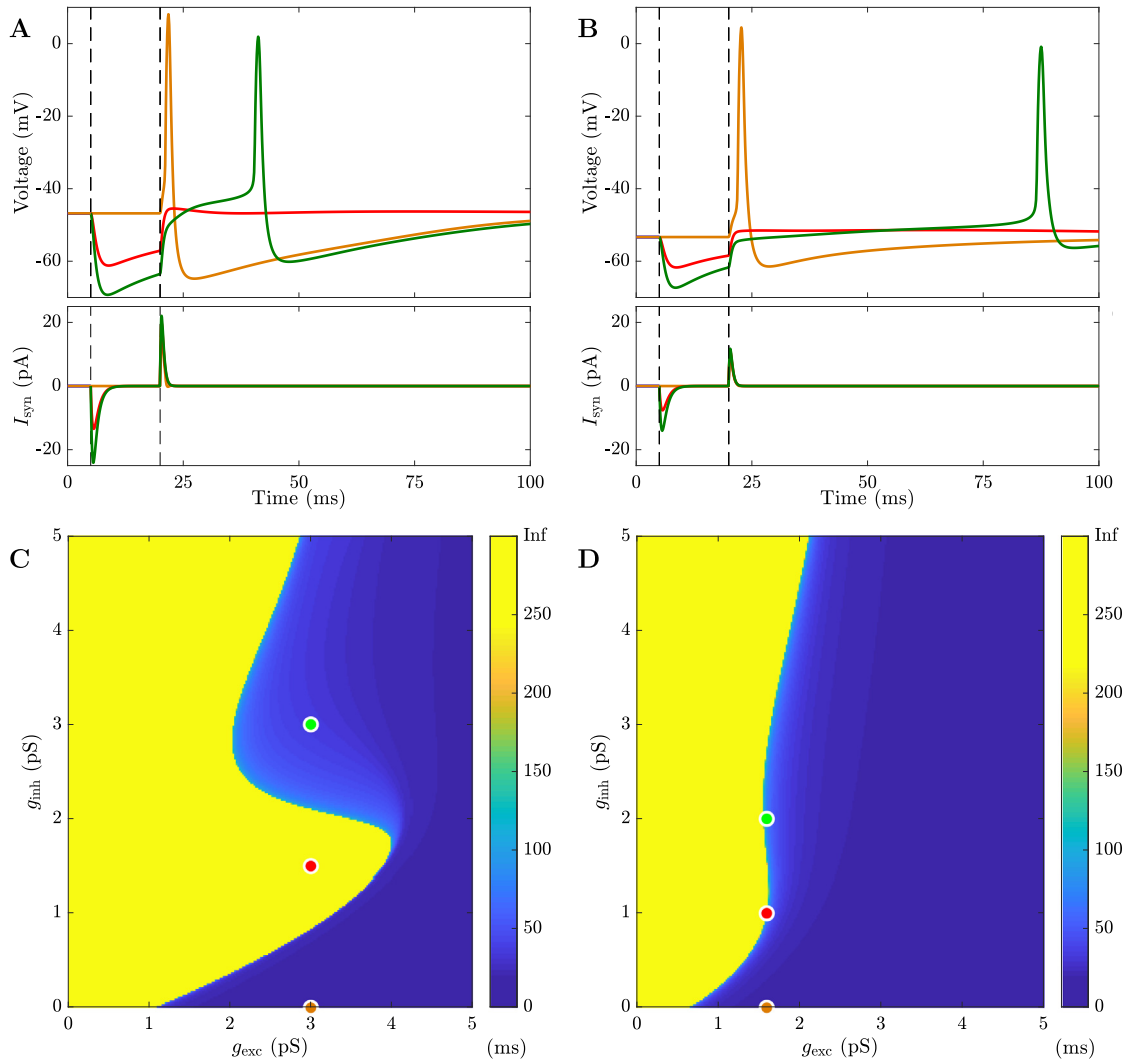
Fig. 12. Responses of stellate cell model to a combination of inhibitory/excitatory (IPSI/EPSI) inputs. Applying a pair of IPSI/EPSI to the stellate cell model during **A**) pre- and **B**) post-runup, separated by 15 ms duration (bottom), evokes different types of responses (top). Three combinations are injected into the revised model during pre- and post-runup: $g_{inh} = 0, 1.5, 3$ pS and $g_{exc} = 3$ pS in **A** and $g_{inh} = 0, 1, 2$ pS and $g_{exc} = 1.6$ pS in **B**. The middle g_{inh} evokes no AP (red), but the first (orange) and last (green) pairs do. In the (g_{exc}, g_{inh})-plane, two parameter regimes associated with the **C**) pre- and **D**) post-runup models are identified based on the types of activity: a non-responsive regime exhibiting no spiking activity (yellow), and a responsive regime exhibiting spiking activity color-coded based on the duration of first-spike latency defined by the color-bar. The orange, red and green dots in **C** and **D** represent the values used in **A** and **B**, respectively. The red dots are in the yellow regimes (non-responsive) while the orange and green dots are in the blue regimes (responsive). (For interpretation of the references to colour in this figure legend, the reader is referred to the web version of this article.)

4. Discussion

4.1. Excitability in stellate cells: runup and latency

In this study, we devised a revised Hodgkin–Huxley type model developed in [5,23] to study two important features of excitability in cerebellar stellate cells; namely, runup in which firing frequency/threshold temporally increases/decreases, respectively, following breakthrough into whole-cell patch-clamp configuration, and the non-monotonic first-spike latency profile when plotted as a function of the holding potential. The model consisted of five ionic currents, including I_{Na}, I_K, I_A, I_T and I_L, that were previously adapted to capture both pre- and post-runup voltage-clamp data [3]. The model was analyzed using bifurcation analysis and numerical computations to unravel the dynamics of these two phenomena, and to answer the fundamental question of how latency manifests itself in the context of runup. The two main findings of the study were that (i) the stellate cell model is a type I oscillator, possessing a saddle-node on an invariant cycle (SNIC) bifurcation (formed by the coalescing of the saddle-node with a homoclinic orbit) which acts as a "threshold" for tonic firing, rather

than a type II oscillator (possessing a Hopf bifurcation), and (ii) the SNIC along with the ghost of the SNIC play key roles in defining dynamics. When plotting the membrane voltage as a function of I_{app} in a bifurcation diagram, the SNIC was more left-shifted with respect to I_{app} in the post-runup case when compared to the pre-runup case, making the former more sensitive to injected depolarizing currents than the latter. Nonetheless, in both cases, the closer these depolarizing currents I_{app} were to I_{SNIC} the lower the frequency of firing produced by the model, gradually approaching zero as $I_{app} \longrightarrow I_{SNIC}^+$ (i.e., when moving towards the homoclinic orbit). The ghost of the SNIC, on the other hand, allowed the formation of slow regions in the phase space that affected first-spike latencies in response to current-step protocol during runup.

4.2. Ionic currents and type I excitability

It has been previously shown that excitable cells expressing A-type K^+ channels can monotonically prolong first-spike latency in response to the step-current of increasingly more negative hyperpolarizing bias-currents. Although stellate cells do express fast inactivating A-type K^+ channels, their first-spike latency profiles, plotted as a function of the holding potential, were shown to be non-monotonic, peaking around ~-55 mV and ~-60 mV during pre- and post-runup, respectively. The main reason for observing such behavior in these cells is because they also express low threshold T-type Ca^{2+} channels which possess activation and inactivation kinetics that are more left-shifted compared to those for A-type K^+ channels. This discrepancy between A-type K^+ and T-type Ca^{2+} channels (particularly in the inactivation kinetics) allows stellate cells to decrease their first-spike latency upon hyperpolarization with currents that keep the membrane voltage at a more negative potential than ~-55 mV (~-60 mV) due to the recruitment of more T-type than A-type channels [5,23]. The firing frequency of these cells is, however, monotonic, linearly decreasing to a very low level (≈ 0) as the amplitude of the applied current is decreased [23]. These results are consistent with our findings that stellate cells exhibit dynamics consistent with type I excitability.

The inclusion of both A-type K^+ and T-type Ca^{2+} currents in the model was a necessary step to generate type I excitability. Excluding the T-type Ca^{2+} current from the model would have made it type II oscillator similar to that developed for motoneurons in aplysia [29]. In that latter model, the ramp phenomenon, in which trajectories travel along the unstable steady state for extended period of time after crossing the Hopf bifurcation, produced the prolonged latencies seen in these cells (provided that the inactivation time constant of A-type K^+ channels is large). Interestingly, motoneurons also exhibit non-monotonic latency profile when plotted as a function of the stimulus time (rather than the holding potential), defined as the time between the brief stimulus and the time of the depolarizing steady applied current upon which the brief stimulus was superimposed. Although these two features in motoneurons (the ramp and non-monotonic first-spike latency) appear quite similar to those seen in stellate cells, they are both very different in how they are dynamically generated.

4.3. Role of the slow region associated with the SNIC in defining dynamics in type I oscillators

Previous studies have shown that SNICs are associated with slow regions (also called ghost of the SNIC) that form whenever $0 < (I_{app}/I_{SNIC}) - 1 \ll 1$. Within these regions in the phase space, solution trajectories travel significantly slower than when they do outside. Passage time in these regions is proportional to $1/\sqrt{|I_{app} - I_{SNIC}|}$ [15], while firing frequency close to the SNIC is proportional to $\sqrt{|I_{app} - I_{SNIC}|}$ [10,27]. Due to the fact that the underlying dynamics of stellate cells are governed by a SNIC bifurcation, solution trajectories defined by the state variables of the Hodgkin–Huxley type model may also propagate through the slow region when they are exposed to a depolarizing test-current following a hyperpolarizing bias-current. The distance from the attractor along with the passage through the slow region determine how long trajectories spend to reach the attractor (the periodic orbit defining the AP-cycle). We showed that altering the bias-current changes the holding potential of the stellate cell model and thus the IC of the solution trajectory. This subsequently makes some trajectories pass through the slow region but remain close to the attractor, pass through the slow region and be far from the attractor, or be far from the attractor but never pass though the slow region. The combination of holding potentials (ICs) eventually result in producing the non-monotonic profile in latency observed in stellate cells.

According to the analysis of the model, first-spike latency becomes shorter for moderate holding potentials and longer for very hyperpolarized holding potentials during runup, but the non-monotonic profile persists during runup, even though the kinetics of Na^+ and A-type K^+ are altered. This is to be expected in view of the fact that the SNIC bifurcation is present in both cases. However, the dynamics associated with pre- and post-runup are not exactly identical. In the pre-runup case, for example, first-spike latency remains finite as $I_{test} \longrightarrow I_{SNIC}^+$ for an extended range of $I_{app} = I_{bias}$, unlike the post-runup case in which only those latencies associated with holding potentials in a very limited interval of holding potentials remain finite as $I_{test} \longrightarrow I_{SNIC}^+$. The location of the IC, determined by the membrane holding potential set by I_{bias}, relative to the stable manifold of the saddle node controls if latencies become infinitely large or not. Those that lie to the left of the stable manifold propagate and generate action potential with finite latencies, while those to the right, land on the stable manifold of the saddle node as $I_{test} \longrightarrow I_{SNIC}^+$. In the pre-runup case, for holding potentials beyond the non-monotonic component of profile, all ICs lie to the left of the stable manifold, whereas in the post-runup case, ICs lie to the left of the stable manifold of the saddle node only for a limited range of I_{bias} near the local minima of the latency profile. From the fact that it is possible for ICs to lie even to the left of the stable manifold of the saddle (when $I_{test} < I_{SNIC}$), we can conclude that runup stellate cells are even capable of generating transient single spikes. The latencies of such transient spikes become

arbitrarily large as $I_{test} \to I_{SIMS}^+$. This result thus indicates that crossing the SNIC is a sufficient condition for generating an AP but not necessary. The dynamics governing these transient spikes differ from those associated with type II and type III excitability [22,27,28] as well as from single bursts generated near a SNIC in response to an inhibitory brief current pulse [6]. Detecting these transient single spikes in electrophysiological recordings of stellate cells remains to be seen.

4.4. Inhibitory/excitatory synaptic inputs in stellate cells

The response of stellate cells to step-currents in vitro provides very valuable information about their dynamics. For in vivo synaptic inputs, the response of these cells may differ significantly due to the fact that such dynamic inputs also possess time constants that will affect the activation/inactivation of various ion channels. In [23], it was shown that applying a pair of inhibitory and excitatory post-synaptic inputs (IPSI and EPSI, respectively) to stellate cells separated by 15 ms in vitro and in silico produces APs if the amplitude of the IPSI is small or large but not intermediate (while keeping the amplitude of the EPSI fixed). The revised model presented here can also produce that type of behavior during pre- and post-runup over an extended range of EPSI amplitudes (g_{exc}). Indeed, in the two-parameter space defined by g_{inh}, g_{exc}, two regimes of behavior were identified, an responsive regime and a non-responsive regime separated by a boundary near which latencies become infinitely large. The folds formed by the boundary between the two regimes are more pronounced in the pre-runup case than post-runup case, allowing for more robust switching between them. Interestingly, the time duration separating the IPSI and EPSI played a minor role in altering the shapes of these boundaries during pre- and post-runup, but affected the latencies of APs formed (results not shown).

Based on the results presented above, one would expect that the amplitude of IPSI along with the delay between IPSI and EPSI specify the holding potential of the cell and subsequently determine if the neuron fires or not, but that is not what we observe. In fact, comparing the response of the stellate cell model (pre- and post-runup) to an intermediate IPSI followed by an EPSI, to that with large IPSI followed by the same EPSI, we find that the membrane voltage exhibits less depolarization in the plateau response prior to firing in the latter case compared to the depolarization seen in the former case, even though no AP is evoked. This makes the notion of a voltage threshold for firing not clearly well-defined here. We hypothesize that the stable manifold of the saddle is responsible for producing this phenomenon. To test this hypothesis, one needs to first reduce the revised model to at most three dimensions and perform time-scale separation in order to apply slow-fast analysis. The resulting analysis can then be used to compute the stable manifold of the saddle, using a two-point boundary value problem, and clarify how the latter affects AP firing. Applying such approach will help define both the voltage threshold in stellate cells in response to synaptic inputs and the boundary between the responsive and non-responsive regimes in (g_{exc}, g_{inh})-plane.

Acknowledgments

References

[1] Alcami P, Franconville R, Llano I, Marty A. Measuring the firing rate of high-resistance neurons with cell-attached recording. J Neurosci 2012;32(9):3118–30.
[2] Alexander RPD, Mitry J, Farjami S, Khadra A, Bowie D. Data from: modeling excitability in cerebellar stellate cells: temporal changes in threshold, latency and frequency of firing. Anmar Khadra Repository 2019; 2019. Deposited July 15th http://www.medicine.mcgill.ca/physio/khadralab/code_CNSNS1.html.
[3] Alexander RPD, Mitry J, Sareen V, Khadra A, Bowie D. Cerebellar stellate cell excitability is coordinated by shifts in the gating behavior of voltage-gated Na$^+$ and A-type K$^+$ channels. eNeuro 2019;6(3):1–17. doi:10.1523/ENEURO.0126-19.2019. https://www.eneuro.org/content/6/3/ENEURO.0126-19.2019.
[4] Anderson D, Engbers JDT, Heath NC, Bartoletti TM, Mehaffey WH, Zamponi GW, et al. The Cav3-Kv4 complex acts as a calcium sensor to maintain inhibitory charge transfer during extracellular calcium fluctuations. J Neurosci 2013;33(18):7811–24. doi:10.1523/JNEUROSCI.5384-12.2013. http://www.ncbi.nlm.nih.gov/pubmed/23637173.
[5] Anderson D, Mehaffey WH, Iftinca M, Rehak R, Engbers JDT, Hameed S, et al. Regulation of neuronal activity by Cav3-Kv4 channel signaling complexes. Nat Neurosci 2010;13(3):333–7. doi:10.1038/nn.2493.
[6] Barnett WH, Cymbalyuk GS. A codimension-2 bifurcation controlling endogenous bursting activity and pulse-triggered responses of a neuron model. PLoS ONE 2014;9(1):e85451.
[7] Bertram R, Butte MJ, Kiemel T, Sherman A. Topological and phenomenological classification of bursting oscillations. Bull Math Biol 1995;57(3):413–39.
[8] Carter AG, Regehr WG. Quantal events shape cerebellar interneuron firing. Nat Neurosci 2002;5(12):1309–18.
[9] Doiron B, Laing C, Longtin A, Maler L. Ghostbursting: a novel neuronal burst mechanism. J Comput Neurosci 2002;12(1):5–25.
[10] Ermentrout B. Linearization of F-I curves by adaptation. Neural Comput 1998;10(7):1721–9.
[11] Ermentrout GB, Terman DH. Mathematical foundations of neuroscience, 35. Springer Science & Business Media; 2010.
[12] Gaffield MA, Christie JM. Movement rate is encoded and influenced by widespread, coherent activity of cerebellar molecular layer interneurons. J Neurosci 2017;37(18):4751–65.
[13] Häusser M, Clark BA. Tonic synaptic inhibition modulates neuronal output pattern and spatiotemporal synaptic integration. Neuron 1997;19(3):665–78.
[14] Izhikevich EM. Neural excitability, spiking and bursting. Int J Bifurcation Chaos 2000;10(06):1171–266.
[15] Izhikevich EM. Dynamical systems in neuroscience. MIT Press; 2007.
[16] Jörntell H, Bengtsson F, Schonewille M, De Zeeuw CI. Cerebellar molecular layer interneurons–computational properties and roles in learning. Trends Neurosci 2010;33(11):524–32.
[17] Kanold PO, Manis PB. Encoding the timing of inhibitory inputs. J Neurophysiol 2005;93(5):2887–97.

[18] Laing CR, Doiron B. Ghostbursting: the role of active dendrites in electrosensory processing. In: Bursting: the genesis of rhythm in the nervous system. World Scientific; 2005. p. 145–72.

[19] Llano I, Marty A. Presynaptic metabotropic glutamatergic regulation of inhibitory synapses in rat cerebellar slices. J Physiol 1995;486(1):163–76.

[20] MacLean JN, Zhang Y, Johnson BR, Harris-Warrick RM. Activity-independent homeostasis in rhythmically active neurons. Neuron 2003;37(1):109–20.

[21] Meisel C, Klaus A, Kuehn C, Plenz D. Critical slowing down governs the transition to neuron spiking. PLoS Comput Biol 2015;11(2):e1004097.

[22] Meng X, Huguet G, Rinzel J. Type III excitability, slope sensitivity and coincidence detection. Discrete Continuous Dyn Syst Ser A 2012;32(8):2729–57.

[23] Molineux ML, Fernandez FR, Mehaffey WH, Turner RW. A-type and T-type currents interact to produce a novel spike latency-voltage relationship in cerebellar stellate cells. J Neurosci 2005;25(47):10863–73. doi:10.1523/JNEUROSCI.3436-05.2005. http://www.ncbi.nlm.nih.gov/pubmed/16306399.

[24] Ospeck M. Auditory nerve spike generator modeled as a variable attenuator based on a saddle node on invariant circle bifurcation. PLoS ONE 2012;7(9):e45326.

[25] Palay SL, Chan-Palay V. Cerebellar cortex: cytology and organization. Springer Science & Business Media; 2012.

[26] Pape H, Budde T, Mager R, Kisvarday Z. Prevention of Ca^{2+}-mediated action potentials in gabaergic local circuit neurones of rat thalamus by a transient K^+ current. J Physiol 1994;478(3):403–22.

[27] Rinzel J, Ermentrout GB. Analysis of neural excitability and oscillations. In: Methods in neuronal modeling. MIT Press; 1989. p. 135–69.

[28] Rinzel J, Huguet G. Nonlinear dynamics of neuronal excitability, oscillations, and coincidence detection. Commun Pure Appl Math 2013;66(9):1464–94.

[29] Rush ME, Rinzel J. The potassium a-current, low firing rates and rebound excitation in Hodgkin–Huxley models. Bull Math Biol 1995;57(6):899–929.

[30] Russier M, Carlier E, Ankri N, Fronzaroli L, Debanne D. A-, T-, and H-type currents shape intrinsic firing of developing rat abducens motoneurons. J Physiol 2003;549(1):21–36.

[31] Sherman AS, Ha J. How adaptation makes low firing rates robust. J Math Neurosci 2017;7(1):4–24.

[32] Shibata R, Nakahira K, Shibasaki K, Wakazono Y, Imoto K, Ikenaka K. A-type K^+ current mediated by the kv4 channel regulates the generation of action potential in developing cerebellar granule cells. J Neurosci 2000;20(11):4145–55.

[33] Szapiro G, Barbour B. Multiple climbing fibers signal to molecular layer interneurons exclusively via glutamate spillover. Nat Neurosci 2007;10(6):735–42.